THE JOURNAL OF PHYSICAL CHEMISTRY C

Article

pubs.acs.org/JPCC

Synthesis-Dependent Oxidation State of Platinum on TiO_2 and Their Influences on the Solar Simulated Photocatalytic Hydrogen Production from Water

Sreenivasan Koliyat Parayil,[†] Harrison S. Kibombo,[†] Chia-Ming Wu,[†] Rui Peng,[†] Trevor Kindle,[†] Srujan Mishra,[‡] S. Phil Ahrenkiel,[‡] Jonas Baltrusaitis,[§] Nada M. Dimitrijevic,[∥] Tijana Rajh,[∥] and Ranjit T. Koodali*[,†]

[†]Department of Chemistry, University of South Dakota, Vermillion, South Dakota 57069, United States

[‡]Nanoscience and Nanoengineering Ph.D. Program, South Dakota School of Mines & Technology, Rapid City, South Dakota 57701, United States

[§]Department of Chemical Engineering, University of Twente, 7522 NB, Netherlands

[∥]Chemical Sciences and Engineering Division and Nanoscience and Nanotechnology, Argonne National Laboratory, Argonne, Illinois 60439, United States

Supporting Information

ABSTRACT: Platinized TiO_2 photocatalysts of different compositions of Pt^0 and PtO_2 were prepared by modifying the synthesis procedures. The physicochemical properties of the composite materials were characterized by X-ray photoelectron spectroscopy and high-resolution transmission electron microscopy. Energy dispersive X-ray spectroscopy measurements confirmed the presence of Pt species existing as PtO_2 and/or mixtures of Pt^0 and PtO_2. The composite material, Pt−TiO_2−2%H, contained a high amount of metallic Pt^0 and PtO_2 in close proximity with TiO_2 that promoted an enhanced photocatalytic hydrogen evolution activity under simulated solar light irradiation. Although Pt−TiO_2−2%C and Pt−TiO_2−2%T consisted of similar compositions of PtO_2, these oxidized platinum species seem to appear further apart from TiO_2 in Pt−TiO_2−2%C than Pt−TiO_2−2%T. This caused dramatic variation in their optical behaviors such as strong fluorescence quenching and lower photocatalytic hydrogen evolution activity in the former photocatalyst. A photocatalyst prepared by the conventional photodeposition method was also prepared, characterized, and its photocatalytic activity assessed. This work provides an opportunity to understand the role of PtO_2 for photocatalytic production of hydrogen from platinized TiO_2 composites and the importance of heterojunctions in such photocatalysts for solar energy conversion.

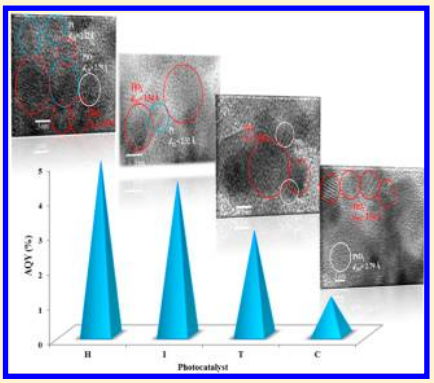

1. INTRODUCTION

Recent research in sustainable energy is focused on the preparation of environmentally benign next generation fuel applications, and hydrogen has emerged as a viable candidate. Hydrogen shows promise as a clean fuel and also as a prevalent element in organic compounds, as it is useful for CO_2 conversion to fuels.[1,2]

Photocatalytic water splitting is a sustainable approach for the production of hydrogen. However, harvesting of solar energy especially visible light radiation is still challenging, and the limitations associated with this process require improved methods and advanced technologies. Fujishima et al. pioneered reports of the photoelectrochemical production of hydrogen from water on TiO_2 electrodes.[3] However, titania is limited in application within the UV region due to the wide band gap. Besides this, the fast electron−hole recombination in TiO_2 is an additional drawback that retards the photocatalytic efficiency. The photoexcitation of TiO_2 requires light with energy greater than or equal to that of its band gap for the generation of electrons and holes.[4] These charge carriers can recombine, get trapped in some metastable surface states, or react with suitable electron donors or acceptors. In the latter process, the charge recombination is minimized, and subsequent photocatalytic reactions occur. Therefore, electron trapping is a critical factor for improving the photocatalytic performance of TiO_2 or its composite derivatives.

It is well documented that the incorporation of a noble metal such as platinum onto the TiO_2 matrix results in photocatalysts that exhibit enhanced activities for various photochemical reactions.[5−16] The presence of Pt species, especially Pt on TiO_2, can retard electron−hole recombination by serving as an electron sink by trapping the photogenerated electrons, and subsequently facilitating the interfacial electron transfer to other electron acceptors.[17,18]

Received: June 10, 2013
Revised: July 25, 2013
Published: July 30, 2013

 © 2013 American Chemical Society

Although it is known that Pt species can exist as Pt^0, Pt^{2+}, and Pt^{4+} or a mixture of these species under various preparative conditions,[11,14,19,20] there is limited literature that is related to the role of oxidized Pt, especially PtO_2 in photocatalytic reactions. Platinized TiO_2 has been explored for several organic degradation studies in which the role of the oxidation state of Pt has been investigated.[21−24] However, such studies have not been explored for solar hydrogen production in detail and are missing in the literature.

Existing reports detailing the use of platinized TiO_2 nanoparticles for photocatalytic hydrogen production especially by water splitting have only focused on factors such as the influence of sacrificial agents,[16] fate of photogenerated electrons,[18] the effects of duration of the reaction,[25] the type of noble metal,[26] the role of the metal loading,[27,28] particle sizes,[29] dispersion,[30] and the effect of pH conditions[31] on the amount of hydrogen evolved. In this respect, detailed studies related to surface composition of Pt or the interaction of these species with TiO_2 still need to be discerned.

Thus, this Article attempts to provide new insight into the efficacy of Pt−TiO_2 materials based on the following facts: (i) a simple method for improving the photocatalytic activity of TiO_2 is presented, (ii) a detailed characterization to understand the surface composition of the metal−oxide materials has been carried out, (iii) knowledge about the controlled synthesis of various Pt species supported on TiO_2, their physicochemical effects, and structure−activity relationships is presented, and (iv) knowledge about the role of the heterojunctions between TiO_2, Pt, and oxidized Pt species in solar hydrogen production is provided; that is, physical insight into the factors affecting the photocatalytic production of hydrogen is presented.

Here, we utilize XPS analysis to clarify the individual role of PtO_2 and explore the influence of the mixture of Pt^0 and PtO_2 species present in the Pt−TiO_2 composite materials synthesized by facile cost efficient sol−gel methods. The effect of such methods for tuning the composition of Pt species, fabricating heterojunctions between Pt species and TiO_2, and their overall influence on solar simulated photocatalytic hydrogen evolution reactions are discussed in detail. Four synthesis methods were utilized for the preparation of Pt−TiO_2 composite materials with different composition of PtO_2 species, and systematically characterized by powder X-ray diffraction (XRD), high-resolution transmission electron microscopy (HRTEM), energy-dispersive X-ray spectroscopy (EDX), EDX mapping, X-ray photoelectron spectroscopy (XPS), electron paramagnetic resonance (EPR), photoluminescence (PL), Raman spectral studies, UV−visible diffuse reflectance spectroscopy (DRS), and N_2 physisorption studies.

2. EXPERIMENTAL SECTION

2.1. Materials. Commercially available titanium isopropoxide ($Ti(^iOPr)_4$, Acros, 98%), methanol (Acros, 99.9% HPLC grade), anhydrous ethanol (Pharmco-AAPER, ACS/USP grade), tetraoctylammonium bromide (TOABr, Alfa Aesar, 98%), hydrogen hexachloroplatinate(IV) hydrate (Acros, ACS grade), potassium tetrachloroplatinate(II) (Pressure Chemical), sodium borohydride (Acros, 98%), 4-dimethyl-aminopydridine (Acros, 99%), cetyltrimethylammonium bromide (CTAB, Acros, ACS grade), toluene (Acros, ACS grade), and concentrated nitric acid (Acros, ACS grade) were used as received. Deionized water with resistivity >18 MΩ cm was used throughout the experiments.

2.2. Synthesis of Pt−TiO_2. *2.2.1. Preparation of Pt−TiO_2−2%H.* 0.30 mL of 0.2 M hydrogen hexachloroplatinate (IV) hydrate solution was dissolved in 18 mL of ethanol under vigorous stirring in a Teflon liner. The hydrolysis process was initiated by the addition of 1 mL of H_2O and catalyzed by the addition of 100 μL of concentrated HNO_3. 2.2 mL of $Ti(^iOPr)_4$ was added dropwise, and the suspensions were left to stir for 3 h to enhance homogeneity and gelation. The resultant gels were subjected to hydrothermal (H) treatment in a Thermolyne autoclave reactor furnace and heated at a temperature of 120 °C for 14 h, filtered, and dried overnight at 70 °C.

2.2.2. Preparation of Pt−TiO_2−2%I. 0.5 g of TiO_2 prepared by hydrothermal method[32] was added to 5−10 mL of ethanol in a Nalgene beaker and stirred for 10 min. 0.34 mL of 0.2 M hydrogen hexachloroplatinate(IV) hydrate corresponding to 2 wt % Pt was added by impregnation (I). Stirring was continued under gentle heating (40−50 °C) for about an hour, and the suspension was left to dry overnight in an oven prior to reduction under H_2 flow. The experiment was repeated by changing the concentration of hydrogen hexachloroplatinate-(IV) hydrate to obtain 0.5 and 1 wt %Pt and labeled as Pt−TiO_2−0.5%I and Pt−TiO_2−1%I, respectively.

2.2.3. Preparation of Pt−TiO_2−2%T. The Pt precursor Pt−TOABr was prepared by a templated (T) phase transfer method reported earlier.[33,34] In a typical synthesis, an appropriate amount of Pt−TOABr corresponding to 2 wt % Pt was dissolved in 18 mL of ethanol under vigorous stirring in Teflon liner. The hydrolysis process was initiated by the addition of 1.65 mL of H_2O followed by the addition of 100 μL of concentrated HNO_3 for catalyzing the reaction. 2.2 mL of $Ti(^iOPr)_4$ was added dropwise, and the suspension was left to stir for 3 h to enhance the homogeneity and gelation. The resultant gel was subjected to hydrothermal treatment in a Thermolyne autoclave reactor furnace and heated at 120 °C for 14 h, followed by cooling, filtering, and drying overnight at 70 °C.

2.2.4. Preparation of Pt−TiO_2−2%C. A precursor Pt-complex solution was prepared by a modified near monodisperse core-like (C) method adopted from previous literature.[35] 4 mL of 50 mM CTAB solution was added to a 50 mL round-bottom flask and stirred at 300 rpm. 5.5 mL of 11.5 mM K_2PtCl_4 was added dropwise at room temperature to obtain a pale orange brown solution. Stirring was continued at 70 °C until a pale solution was obtained. 0.5 mL of 6 mM L-ascorbic acid was then added to reduce the Pt species and obtain a black solution of Pt−CTAB complex. After being stirred for 6 h, 5.8 mL of the complex solution was added dropwise on 0.3 g of TiO_2 prepared previously.[32] The powder obtained was dried overnight at 70 °C, ground well, and calcined in air at 500 °C to remove CTAB.

The powders obtained by the four synthesis methods were ground well and subjected to reduction at 450 °C under H_2 flow for 6 h at a heating rate of 3 °C/min.

2.2.5. Preparation of Pt−TiO_2−2%PD. The Pt−TiO_2−2% PD sample was prepared via photodeposition method in the presence of methanol under the irradiation of UV light in accordance with literature reports.[23] 150 mg of TiO_2 was added into a 5 mL quartz cell. An appropriate amount of Pt source (H_2PtCl_6) that is equivalent to the 2 wt % of weighed TiO_2 was suspended in 3 mL of HPLC grade methanol. After the Pt source was completely dissolved in methanol, the clear solution was poured into the quartz cell and the cell was sealed to be

dx.doi.org/10.1021/jp405727k | J. Phys. Chem. C 2013, 117, 16850−16862

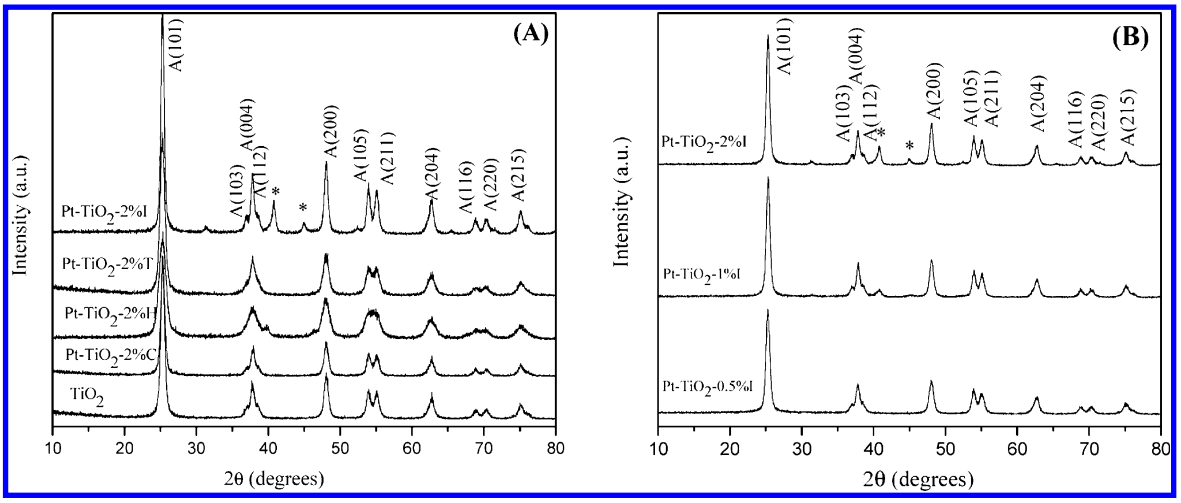

Figure 1. XRD patterns of the Pt−TiO_2 composite materials. (A) Bare TiO_2 is also shown for comparison and (B) XRD patterns of the Pt−TiO_2−I prepared with various composition of Pt loading. The "*" denotes the diffraction peaks due to Pt species.

airtight. The mixed suspension was stirred vigorously to ensure that the TiO_2 and Pt source were mixed well. Later, the quartz cell was purged with argon gas for 30 min to remove air. After degassing, the quartz cell was placed in front of the UV light source for 1 h to photodeposit Pt onto TiO_2. The light source was a 300 W Xe lamp equipped with an optical cutoff filter ($\lambda >$ 280 nm). The reaction proceeded under vigorous stirring using a magnetic stirring rod coated with polytetrafluoroethylene (PTFE).

2.3. Characterization. The XRD measurement was performed at room temperature using a Rigaku Ultima IV X-ray diffractometer with Cu K_α radiation. The diffractometer was operated at 40 kV and 44 mA, scanned with a step size of 0.02° and a count time of 1°/min in the range of 2θ from 10° to 80°. The crystallite sizes of TiO_2 in Pt-TiO_2 were determined by selecting the anatase peaks at 25.3°, 48.1°, and 62.8° using PDXL software (version 1.8.1) provided by Rigaku.

The textural properties, such as surface areas, pore size distributions of TiO_2, and Pt-TiO_2 materials were analyzed by using N_2 physisorption using a NOVA 2200*e* (Quantachrome Instruments) surface area and pore size analyzer. After the materials were dried overnight at 70 °C and degassed extensively at 100 °C prior to the adsorption measurements, the N_2 isotherms were obtained at −196 °C. The surface areas of the synthesized materials were calculated by using the Brunauer−Emmett−Teller (BET) equation within a relative pressure (P/P_0) range of 0.05−0.30. The pore volume was determined from the amount of N_2 adsorbed at the highest relative pressure of $P/P_0 \approx 0.99$. The pore diameter and pore size distribution plots were defined by applying the Barrett−Joyner−Halenda (BJH) model to the desorption isotherm.

The X-ray photoelectron spectroscopic (XPS) measurement was carried out using a custom-designed Kratos Axis Ultra instrument in a surface analysis chamber with monochromatic radiation at 1486.6 eV from an aluminum K_α source using a 500 mm Rowland circle silicon single crystal monochromator. The X-ray gun was operated with a current at 15 mA and at an accelerating voltage of 15 kV. Low energy electrons were used for the charge compensation to neutralize the samples. The samples were transferred to the indium foil and mounted on the copper stub. High-resolution spectra were acquired in the region of interest using 20−40 eV energy windows, pass energy of 20 eV, step size of 0.1 eV, and dwell time of 1000 ms. The absolute energy scale was calibrated to the Cu $2p_{2/3}$ peak binding energy of 932.6 eV using an etched copper plate. All spectra were calibrated using C1s peak at 284.6 eV, and a Tougaard-type background was subtracted from each spectrum.

Prior to TEM and HRTEM analysis, the samples were dispersed in ethanol, and the suspensions were sonicated for an hour. For each material, one drop of suspension was placed on a copper grid coated with carbon film, and allowed to dry overnight. The TEM images were recorded on a Tecnai G^2 instrument operating at 120 kV. The HRTEM measurements were carried out using JEOL JEM-2100 LaB_6 transmission electron microscope, equipped with the high-resolution style objective-lens pole piece to achieve a point resolution as small as 0.23 nm. The instrument was operated at a high tension of up to 200 kV, corresponding to an electron wavelength of 2.5 pm. Image acquisition was performed with a Gatan Orius bottom-mount, 14-bit, 11-megapixel CCD camera. An Oxford Inca energy-dispersive silicon-drift X-ray (EDX) spectrometer was provided for compositional analysis and mapping at high count rates.

Raman spectra were collected using a Horiba Jobin Yvon Labram Aramis Raman spectrometer with a He−Ne laser (532 nm) as the light source. The unfiltered beam of scattered laser radiation was focused onto the samples through a microscope objective (×50) for an acquisition time of 5 s and repetition of 10×. The radiation was dispersed by an 1800 line/mm grating onto a CCD detector, and at a laser power output of 0.83 mW.

The UV−vis diffuse reflectance spectra (DRS) were collected by a Cary 100 Bio UV−visible spectrophotometer with a praying mantis diffuse reflection accessory (Harrick Scientific).

The X-band continuous wave electron paramagnetic resonance (EPR) experiments were conducted on a Bruker Elexsys E580 spectrometer equipped with Oxford CF935 helium flow cryostat with ITC-5025 temperature controller. Samples dispersed in 1:1 glycerol/H_2O were purged with argon and illuminated at 77 K, and EPR spectra were recorded at 5 K immediately after illumination. A 300 W Xe UV lamp (ILC) equipped with IR filter was used as the light source. The *g* factors were calibrated for homogeneity and accuracy by comparison to a coal standard, $g = 2.00285 \pm 0.00005$.

Photoluminescence (PL) measurements were carried out on a Horiba Jobin Yvon-Fluoromax4. The excitation wavelength

dx.doi.org/10.1021/jp405727k | J. Phys. Chem. C 2013, 117, 16850−16862

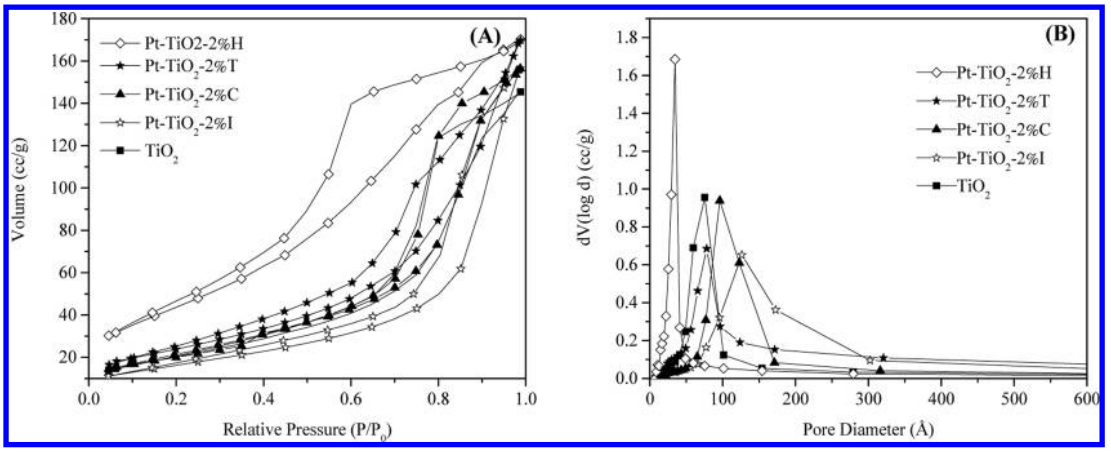

Figure 2. (A) N_2 sorption isotherms and (B) pore size distributions of the Pt−TiO_2 materials. Bare TiO_2 is also shown for comparison.

used was 385 nm, and the emission spectra were monitored in the 400−500 nm range.

2.4. Photocatalytic Water Splitting. Photocatalytic hydrogen evolution reactions were carried out in a quartz reactor as described previously by us.[32,36,37] Typically, a known amount of the photocatalyst was suspended in a solution of H_2O (1 g/L) and methanol (molar ratio of $[H_2O]/[CH_3OH]$ = 8). The suspension was degassed for 30 min with high-purity argon prior to irradiation. The samples were continuously stirred throughout the course of the experiment. A 300 W xenon lamp (Oriel light source) provided simulated solar radiation through a 1.5 air mass (A.M.) filter. The amount of H_2 produced was measured by gas chromatography (SRI 8610 C) equipped with a molecular sieve column and a TCD detector, and by using a calibration curve prepared previously. We have detected formaldehyde in our experiments but have not quantified it because it is not the focus of this work.

3. RESULTS AND DISCUSSION

3.1. Powder X-ray Diffraction Studies. The X-ray powder diffraction patterns of Pt−TiO_2 composites prepared under various methods are shown in Figure 1A. All of the samples exhibited diffraction peaks due to d_{101}, d_{104}, d_{200}, d_{105}, d_{211}, and d_{204} at 2θ values of 25.3°, 37.8°, 48.1°, 53.9°, 55.1°, and 62.8° of the anatase crystal phase, respectively. The addition of Pt species to TiO_2 results in Pt−TiO_2−2%T and Pt−TiO_2−2%C materials whose diffraction patterns are similar to that of TiO_2 where the anatase phase is predominant. The peak corresponding to Pt species is not observed probably due to small size and high dispersion of Pt in these composite materials. The samples Pt−TiO_2−2%H and Pt−TiO_2−2%I exhibit peaks at 2θ = 41° and 46° that correspond to the presence of Pt^0 species.[34]

The calculated crystallite sizes of TiO_2 in Pt−TiO_2 were found to be comparable and approximately 7 ± 1, 10 ± 1, 12 ± 2, 14 ± 2, and 12 ± 2 nm for Pt−TiO_2−2%H, Pt−TiO_2−2%T, Pt−TiO_2−2%C, Pt−TiO_2−2%I, and pure TiO_2, respectively. The sample Pt−TiO_2−2%PD showed peaks due to the anatase phase similar to the other four samples. The crystallite size of titania in this material was estimated to be 12 ± 2 nm. However, peaks due to Pt species could not be seen in this sample either due to their small size and good dispersion as in the cases of the samples Pt−TiO_2−2%T and Pt−TiO_2−2%C.

To understand the role of PtO_2 on TiO_2 and optimize the physical properties related to PtO_2 loading, two additional photocatalysts were prepared using the impregnation method. The powder XRD patterns of Pt−TiO_2−I prepared with 0.5, 1, and 2 wt % of Pt are shown in Figure 1B. The materials exhibited diffraction peaks due to d_{101}, d_{104}, d_{200}, d_{105}, d_{211}, and d_{204} at 2θ values of 25.3°, 37.8°, 48.1°, 53.9°, 55.1°, and 62.8° due to the anatase crystal phase. The 0.5 wt % Pt sample shows peaks only due to the anatase phase of titania. A further increment in loading to 1 and 2 wt % results in materials that exhibit peaks at 2θ = 41° and 46°. These additional peaks correspond to Pt^0.

3.2. N_2 Isotherms and Pore Size Distributions. The N_2 isotherms of the Pt−TiO_2 composites and the bare TiO_2 are examined as shown in Figure 2A to understand the textural properties of Pt−TiO_2 composite materials.

The materials exhibit type IV isotherms of mesoporous materials according to IUPAC classification.[38] The initial part of the isotherm is due to monolayer adsorption at low values of relative pressures (P/P_0), followed by multilayer adsorption and capillary condensation. All of the materials exhibit H3 type hysteresis loops that do not level off at relative pressures close to the saturation vapor pressure, suggesting that the materials are composed of loose assemblies of irregular shaped plate-like particles forming slit-like pores of broad pore size distribution.[39] The amount of adsorbate appears to vary due to the differences in porosities, and a resultant difference in surface area is obtained.

The specific surface area calculated from the BET adsorption isotherm for TiO_2 is 65 $m^2\ g^{-1}$. The method used to incorporate Pt with the support appears to influence the resultant surface areas achieved. A 2 wt % loading of platinum results in an increase in the surface area to 74, 89, 167 $m^2\ g^{-1}$ from the core-like (C), templated (T), and hydrothermal (H) methods, respectively. The material prepared by the impregnation (I) method appears to maintain a surface area comparable to that of TiO_2 at ca. 62 $m^2\ g^{-1}$. For the high surface area material, Pt−TiO_2−2%H, Pt precursor was added to the reaction mixtures prior to hydrothermal treatment, which minimizes agglomeration of particles and facilitates their access to the pores of the mesostructure as reported previously.[34] This change is supported by the slightly lower crystallite size (7 ± 1 nm) of TiO_2 as determined by XRD. Hence, this material shows higher surface area (167 m^2/g) as compared to the other Pt−TiO_2 composite materials and exhibits unique pore size characteristics with ordered set of mesopores centered at 49 Å as shown in Figure 2B, which is much smaller than the 76 Å

dx.doi.org/10.1021/jp405727k | J. Phys. Chem. C 2013, 117, 16850−16862

Table 1. Textural Properties of Pt−TiO_2 Composite Materials

materials	S_{BET}[a] (m^2 g^{-1})	pore volume (cm^3 g^{-1})	PD[b] (Å)	TiO_2 size (±1 nm)	band gap[c] (eV)	H_2[d] (mmol g^{-1})	AQY[e] (%)
TiO_2	65	0.23	76	12	3.2	1.4	1.1
Pt−TiO_2−2%H	167	0.26	49	7	3.3	6.3	5
Pt−TiO_2−2%C	74	0.24	77	12	3.2	1.3	1.1
Pt−TiO_2−2%T	89	0.26	79	10	3.2	3.7	3
Pt−TiO_2−2%I	62	0.24	127	14	3.4	5.4	4.4
Pt−TiO_2−1%I	71	0.26	127	13	3.4	5.8	4.7
Pt−TiO_2−0.5%I	80	0.28	124	12	3.2	7.5	6.1

[a]Surface area determined by applying Brunauer−Emmett−Teller (BET) equation to a relative pressure (P/P_0) range of 0.05−0.35 of the adsorption isotherm. [b]Pore diameter is calculated from the Barrett−Joyner−Halenda (BJH) equation using the desorption isotherm. [c]Band gap energies estimated from Tauc plots. [d]Values depict photocatalytic efficiencies after 4 h under simulated solar light irradiation conditions. [e]Apparent quantum yield.

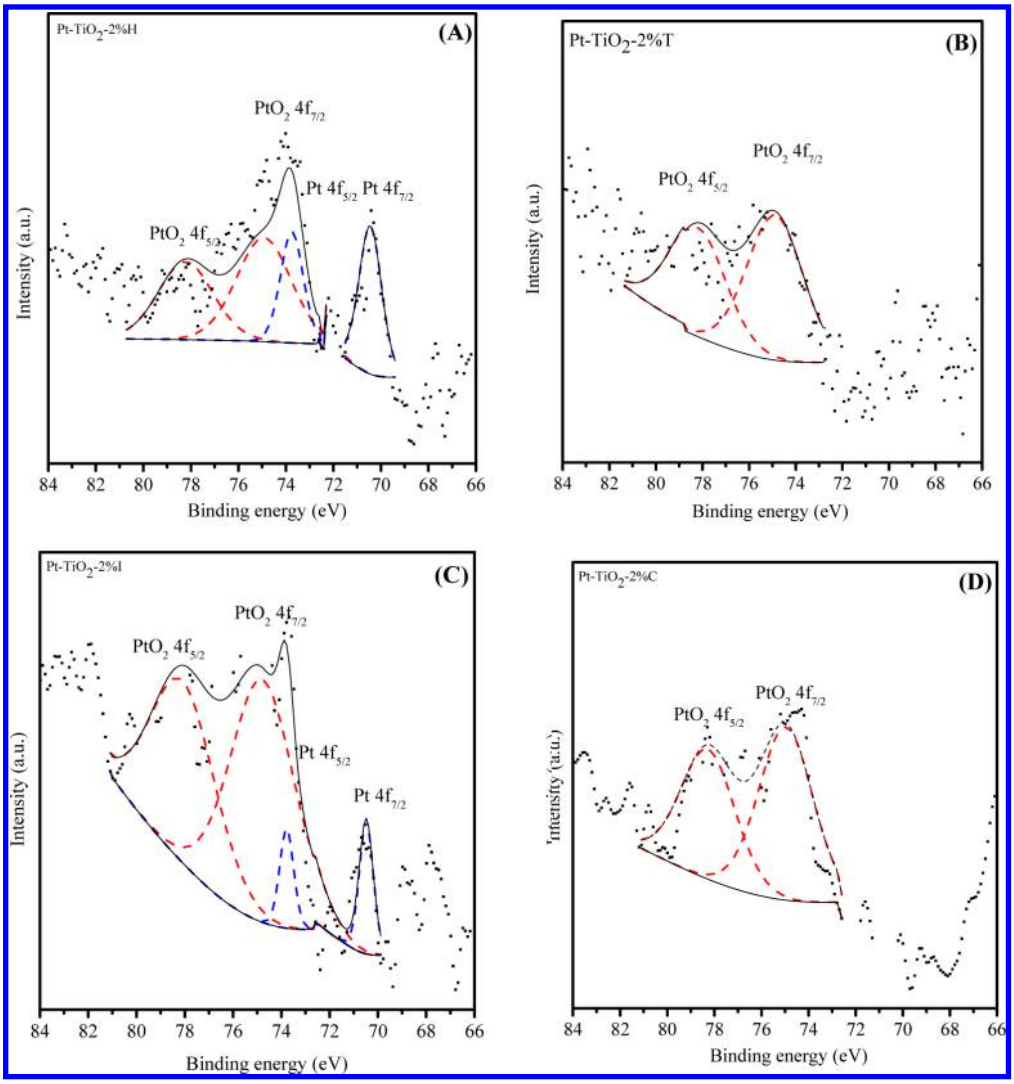

Figure 3. XPS for Pt 4f spectral regions in (A) Pt−TiO_2−2%H, (B) Pt−TiO_2−2%T, (C) Pt−TiO_2−2%I, and (D) Pt−TiO_2−2%C.

observed for TiO_2. Pt−TiO_2−2%T, Pt−TiO_2−2%C, and Pt−TiO_2−2%I exhibit pores centered at 77, 97, and 127 Å, respectively. The textural properties, including specific surface area, pore volumes, and BJH pore diameters obtained for the Pt−TiO_2 materials studied in this work, are summarized in Table 1.

To understand the variation in textural properties due to PtO_2 on TiO_2, we carried out the N_2 isotherm analysis of Pt−TiO_2−I with 0.5, 1, and 2 wt % of Pt loading. The isotherms of the materials exhibited type IV with H3 type hysteresis loops and are displayed in Figure S1 of the Supporting Information.

The sample Pt−TiO_2−2%PD also exhibited type IV isotherm with H3 hysteresis loops. It had a surface area of 60 m^2/g, pore volume of 0.12 cm^3/g, and pore diameter centered at 57 Å.

3.3. XPS Studies. Quantitative XPS studies were carried out to determine the oxidation state of surface platinum species and elucidate the influence on hydrogen evolution rates. The survey

dx.doi.org/10.1021/jp405727k | J. Phys. Chem. C 2013, 117, 16850−16862

scans (not shown) indicate the presence of Pt, O, and Ti and adventitious carbon. In addition, TGA results (not shown) suggest the absence of residual organics or surfactants. Figure 3A–D shows the XPS spectra of Pt–TiO_2–2%H, Pt–TiO_2–2%T, Pt–TiO_2–2%I, and Pt TiO_2–2%C in the Pt 4f region, respectively. It has been reported that Pt^0 exhibits Pt $4f_{7/2}$ and Pt $4f_{5/2}$ bands in the ranges of 70.2–71.0 and 73.6–74.0 eV, respectively.[5,10] Similarly, Pt^{4+} has been reported to exhibit Pt $4f_{7/2}$ and Pt $4f_{5/2}$ bands in the regions of ca. 74.6–75.8 and 76.5–78.2 eV, respectively.[12,40] Accordingly, the $4f_{7/2}$ binding energies of Pt and PtO_2 were constrained at 70.4 ± 0.1 and 74.8 ± 0.1 eV, respectively. All of the peaks used for quantification were Gaussian/Lorentzian shape GL (30:70) curves with equivalent eV at the full-width-half-maximum (fwhm). From XPS analysis, we can deduce that the synthetic methods of choice influence the resultant oxidation state of Pt. The materials prepared by the hydrothermal treatment and impregnation methods display peaks that correspond to Pt^0 and Pt^{4+} (PtO_2) as seen by the profiles of Pt–TiO_2–2%H and Pt–TiO_2–2%I, respectively. However, in Pt–TiO_2–2%C and Pt–TiO_2–2%T, the only peak present is that associated with Pt^{4+} probably as a result of the complete oxidation of Pt species in these materials. Even though both of these composites consist of similar amount of Pt species (100% PtO_2), the interaction of TiO_2 with PtO_2 may be different as evidenced later in this Article. More details of the distribution of Pt species in these materials are shown in Table 2.

Table 2. XPS Spectral Regions for Pt Species Present in Pt–TiO_2 Composite Materials

	Pt^0 (eV)		PtO_2 (eV)				
materials	Pt $4f_{7/2}$	Pt $4f_{5/2}$	Pt $4f_{7/2}$	Pt $4f_{5/2}$	Pt^0 wt %	PtO_2 wt %	PtO_2/Pt^0
Pt–TiO_2–2%H	70.4	73.7	74.9	78.2	37.3	62.7	1.7
Pt–TiO_2–2%C			74.8	78.1		100	∞
Pt–TiO_2–2%T			74.9	78.2		100	∞
Pt–TiO_2–2%I	70.5	73.8	74.8	78.1	10.7	89.3	8.3
Pt–TiO_2–1%I	70.4	73.7	74.8	78.1	11.1	88.9	8.0
Pt–TiO_2–0.5%I	70.3	73.6	74.7	78.0	7.6	92.4	12.2
Pt–TiO_2–2%PD	70.4	73.7	74.8	78.1	50.5	49.5	0.98

The Ti and O regions for all of the composite materials were found to be similar, and the high-resolution XPS spectrum of the Ti 2p regions of a representative sample, Pt–TiO_2–2%H, is shown in Figure 4A. Two intense peaks at 458.7 and 464.5 eV that correspond to the Ti $2p_{3/2}$ and Ti $2p_{1/2}$ binding energy regions were observed. They indicate the presence of Ti^{4+} ions in TiO_2. Furthermore, Figure 4B displays spectra corresponding to the O 1s region that reveal the presence of two peaks due to Ti–O bond (529.5 eV) and O–H bond (531.4 eV), respectively.

The XPS study of Pt–TiO_2–2%PD indicates the presence of both Pt and PtO_2 at similar binding energies to the rest of the four materials in this study. Bands ($4f_{7/2}$ and $4f_{5/2}$) at 70.4 and 73.7 eV due to Pt^0, and at 74.8 and 78.1 eV due to Pt^{4+} ($4f_{7/2}$ and $4f_{5/2}$), have been observed in this sample. The wt % of Pt^0 and PtO_2 is estimated to be 50.5% and 49.5%, respectively, as indicated in Table 2.

3.4. Microscopic Studies. XPS provides valuable information regarding oxidation state of the Pt species; however, it is limited as a surface technique and is deficient in providing characteristics pertaining to the location and structural properties of the bulk of the composite materials. Moreover, the location of the catalytically active sites is very important for understanding the photocatalytic activity. Therefore, we carried out a detailed morphological study of these composites.

Because the XPS studies suggested the presence of only PtO_2 species in Pt–TiO_2–2%T and Pt–TiO_2–2%C composites, TEM images were taken at high and low resolution, and the corresponding EDX spectra were compared. Besides these measurements, the EDX elemental mapping was also recorded from selected sample areas for confirming the distribution of Ti, O, and Pt species in the composite materials. Figure 5a shows the HRTEM image of Pt–TiO_2–2%T, which indicates that TiO_2 nanoparticles are in close contact with PtO_2 and viable for the formation of a heterojunction. The anatase TiO_2 phase with *d* spacing of 3.54 Å due to (101) and PtO_2 phase with *d* spacing of 2.79 Å due to (110) spacing is also shown in Figure 5a. However, it is difficult to unambiguously discern the Pt species through the low-resolution TEM image of this material (Figure 5b). Figure 5c displays the EDX spectrum that confirms the presence of Pt species in this sample as indicated by a small peak around 2 KeV. In addition, the presence of Ti and O is also confirmed. The elemental mapping corresponding to O, Ti, and Pt measured from the selected sample area (Figure 5d) is shown in Figure 5e–g, respectively. From the elemental mapping, it is clear that Pt species are within proximity in the selected area as indicated by the similar EDX mapping image of Ti and O. This argument is supported by the HRTEM image shown in Figure 5a.

Similarly, Figure 6 indicates the high- and low-resolution TEM images and the corresponding EDX spectrum for the Pt–TiO_2–2%C composite. Besides these measurements, the elemental mappings are also recorded from selected sample areas for confirming the distribution of Ti, O, and Pt species in the composite materials. Figure 6a and b shows the high- and low-resolution TEM image of Pt–TiO_2–2%C, respectively. The HRTEM indicates that TiO_2 nanoparticles appear distant from PtO_2. The anatase TiO_2 phase with *d* spacing of 3.54 Å due to (101) and PtO_2 phase with *d* spacing of 2.79 Å due to (110) is also shown in Figure 6a. However, it is difficult to discern the Pt species in the low-resolution TEM image of this material (Figure 6b). Even though the EDX spectrum of Pt–TiO_2–2%C shown in Figure 6c is almost identical to that of Pt–TiO_2–2%T, the EDX elemental mapping (Figure 6d–f) indicates that the distribution of the PtO_2 species is entirely different from that in Pt–TiO_2–2%T. The regions are loosely occupied and show apparent voids, which indicates lower interaction between elements in this composite material.

The high- and low-resolution TEM image and the corresponding EDX of other Pt–TiO_2 composite materials are also shown in the Supporting Information (Figures S3 and S4). From the HRTEM image of Pt–TiO_2–2%H, we can observe the anatase TiO_2 phase with *d* spacing of 3.54 Å due to (101), Pt phase with *d* spacing of 2.32 Å due to (111), and the PtO_2 phase with *d* spacing of 2.79 Å due to (110) are in close contact with each other. Hence, we can conclude that there is direct attachment of Pt and PtO_2 species to the TiO_2 surface in this material. The density of Pt species in the selected region is

dx.doi.org/10.1021/jp405727k | J. Phys. Chem. C 2013, 117, 16850–16862

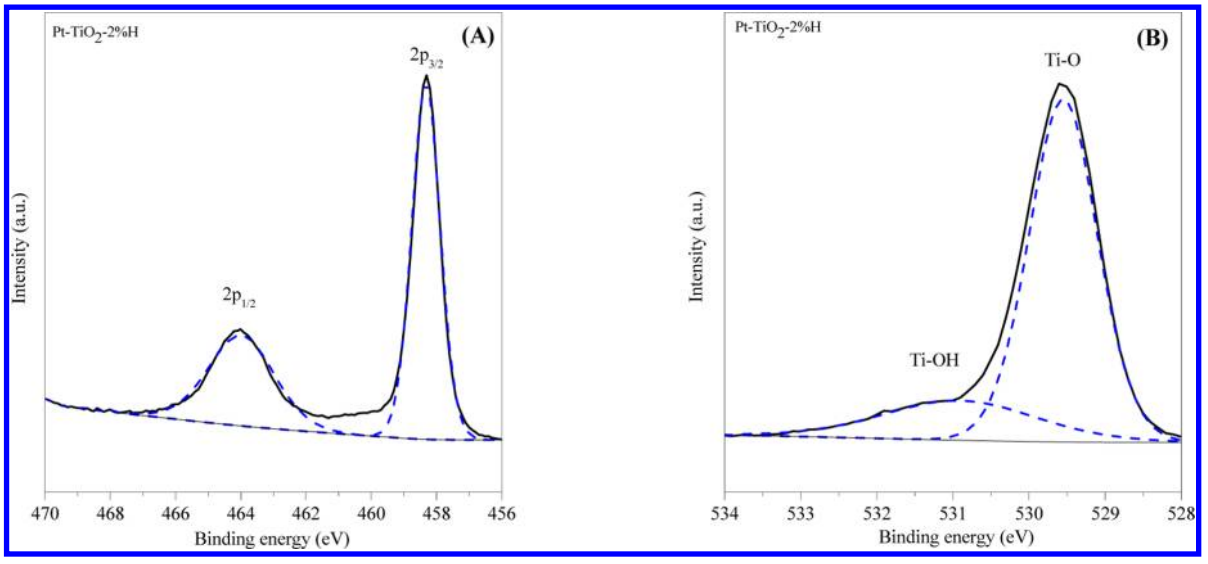

Figure 4. XPS spectral regions for (A) Ti 2p and (B) O 1s in Pt−TiO_2−2%H.

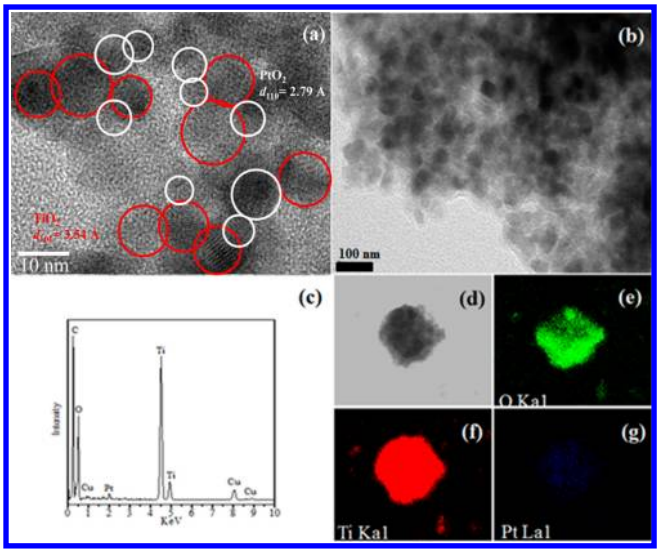

Figure 5. (a) High- and (b) low-resolution TEM images of Pt−TiO_2−2%T. (c) EDX spectrum and corresponding EDX elemental mappings from (d) selected area for (e) O, (f) Ti, and (g) Pt regions.

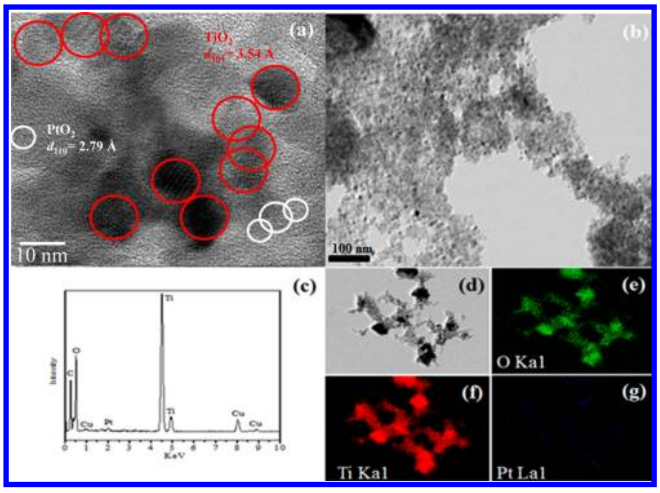

Figure 6. (a) High- and (b) low-resolution TEM images of Pt−TiO_2−2%C. (c) EDX spectrum and corresponding EDX elemental mappings from (d) selected area for (e) O, (f) Ti, and (g) Pt regions.

somewhat similar to that of the Ti and O regions, and indicates the close interaction of these elements in the composite material.

The Pt−TiO_2−2%I also shows the close interaction of Pt and PtO_2 species with TiO_2 in the composite material. Similarly, the small amount of Pt is difficult to discern in the low-resolution TEM. However, from the HRTEM image, we can observe the TiO_2 anatase phase with *d* spacing of 3.54 Å due to (101) and the PtO_2 phase with *d* spacing of 2.79 Å due to (110). Thus, the EDX and HRTEM measurements are useful for supporting the presence of Pt in these composite materials. All of the materials prepared by the four different synthetic methods, and the control prepared by the photodeposition method, show anatase TiO_2 with an average crystallite size of 10 ± 2 nm as shown in Figures 5, 6, S3, S4, and S5, respectively. This is within range and consistent with the crystallite sizes estimated in the powder XRD analysis.

The TEM and EDX image of the photocatalyst, Pt−TiO_2−2%PD, is shown in Figure S5. The presence of multiple heterojunctions between Pt and TiO_2 and PtO_2 and TiO_2 can be visualized in Figure S5(a) and (b).

3.5. Raman Spectroscopic Studies. The XRD studies indicate anatase as the predominant crystal phase for all of the Pt−TiO_2 composite materials prepared. We utilized Raman spectroscopy as a more sensitive technique to confirm the presence of these phases in bare TiO_2 and Pt−TiO_2 composite materials as shown in Figure 7A. The bare TiO_2 shows bands at 141 cm^{-1} (E_g), 193 cm^{-1} (E_g), 393 cm^{-1} (B_{1g}), 513 cm^{-1} (A_{1g}), 519 cm^{-1} (B_{1g}), and 636 cm^{-1} (E_g) attributed to the anatase phase.[36,41,42] After the formation of Pt−TiO_2, all of the Pt−TiO_2 composites show Raman features of anatase phase TiO_2 only, and this supports the XRD results. The absence of peaks due to Pt species may be due to their very small size and high dispersion in the composites. The slight red shift in vibrational features and reduction in intensities of the anatase TiO_2 peaks in Pt−TiO_2 composite may be due to the presence of various Pt species.

To understand the role of pure PtO_2 on TiO_2 and optimize the physical properties, the Raman spectra of a representative PtO_2-containing composite, Pt−TiO_2−I prepared by the

dx.doi.org/10.1021/jp405727k | J. Phys. Chem. C 2013, 117, 16850−16862

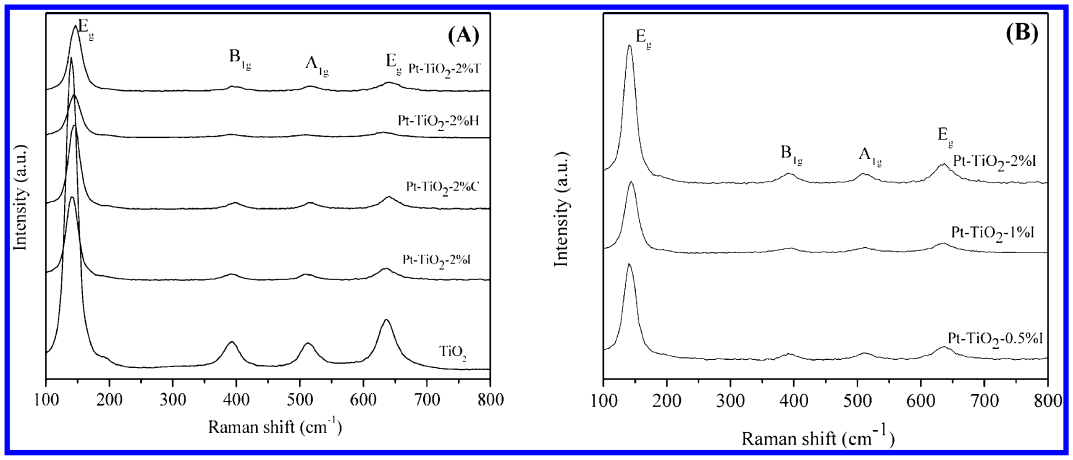

Figure 7. Raman spectra of (A) Pt−TiO_2 composite materials prepared by H, T, C methods and (B) Pt−TiO_2−I with different Pt loading. The spectrum for bare TiO_2 is shown for comparison.

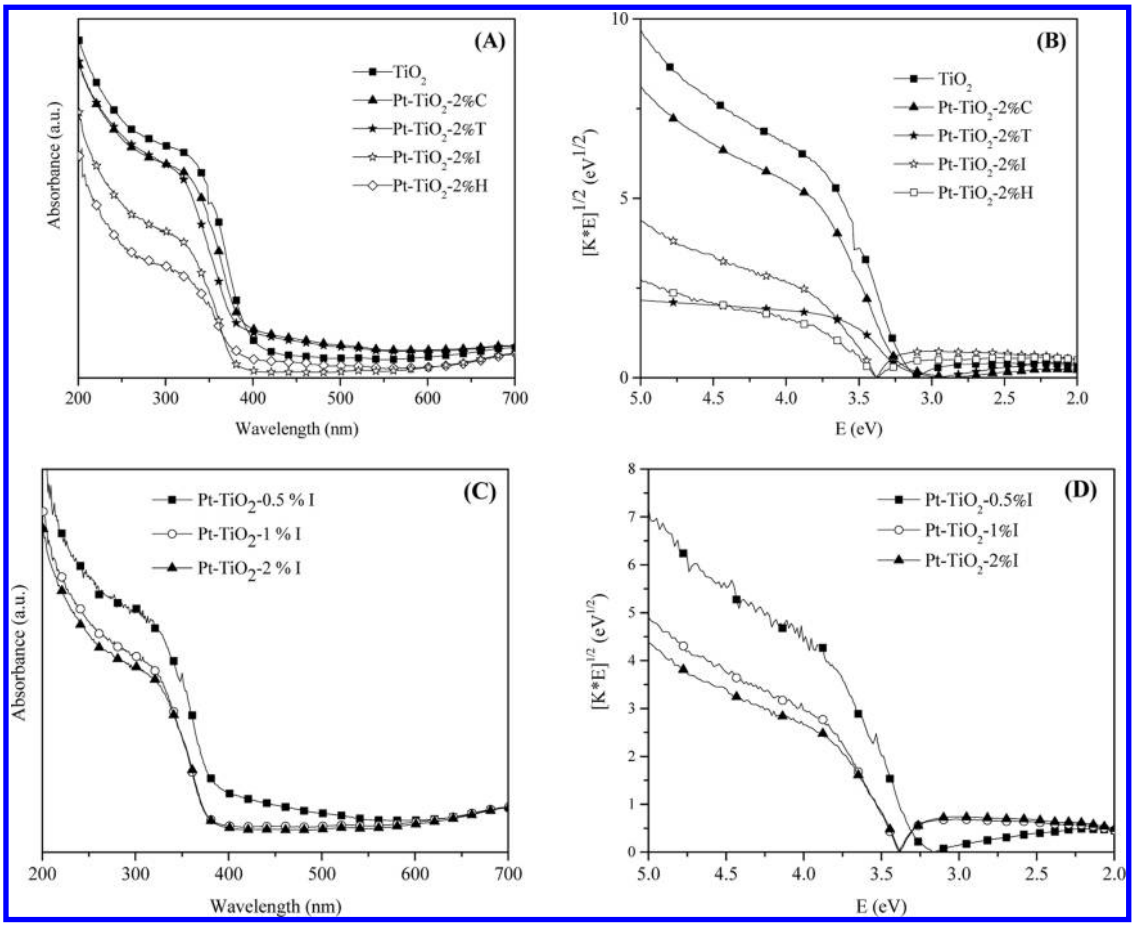

Figure 8. (A) DRS and (B) Tauc plots for Pt−TiO_2 composite materials prepared by H, T, C methods. (C) DRS and (D) Tauc plots for Pt−TiO_2−I with various Pt loading. The bare TiO_2 is also shown for comparison.

impregnation method with different Pt loading, are also shown in Figure 7B. The spectra also show anatase as the predominant crystal phase.

3.6. UV−Vis DRS Studies. UV−visible DRS measurements were carried out to investigate the effect of Pt incorporation on the optical properties of TiO_2, and the spectra are shown in Figure 8A. The absorption spectrum of TiO_2 exhibits a peak below 400 nm, which is typically attributed to the electronic transitions from the valence band to the conduction band of TiO_2. The bandgaps of all of the materials prepared in this study are similar with bandgap values of nearly 3.2 eV. The absorption onset was calculated by using a Tauc plot that is a Kubelka−Munk modified function, $[K^*E]^{1/2}$ against the photon energy, E, measured in eV (Figure 8B). The band gap energy (E_g) was estimated by extrapolating the linear portion of the spectra to $[K^*E]^{1/2} = 0$. The band gap of TiO_2 is estimated to be 3.2 eV, and a slight blue shift in absorption to the UV region with band gaps between 3.3−3.4 eV is observed for Pt−TiO_2−2%H and Pt−TiO_2−2%I. The absorption properties of Pt−TiO_2−2%T and Pt−TiO_2−2%C are identical,

dx.doi.org/10.1021/jp405727k | J. Phys. Chem. C 2013, 117, 16850−16862

and their band gap energies are similar to that of TiO_2. To investigate the influence of PtO_2 alone on the optical properties of Pt−TiO_2, Pt−TiO_2−I was synthesized with different Pt loadings by using the impregnation method, and the DRS are shown in Figure 8C. The corresponding Kubelka−Munk plot is also shown in Figure 8D. The band gap energies calculated for Pt−TiO_2−2%I, Pt−TiO_2−1%I, and Pt−TiO_2−0.5%I are 3.4, 3.4, and 3.2 eV, respectively. The bandgap of Pt−TiO_2−2%PD was estimated to be 3.3 eV.

3.7. Solar Simulated Photocatalytic Hydrogen Evolution. The influence of Pt species in the Pt−TiO_2 composite materials was evaluated by conducting solar hydrogen evolution experiments under simulated light irradiation, and the results are plotted in Figure 9. The apparent quantum yields (AQY)

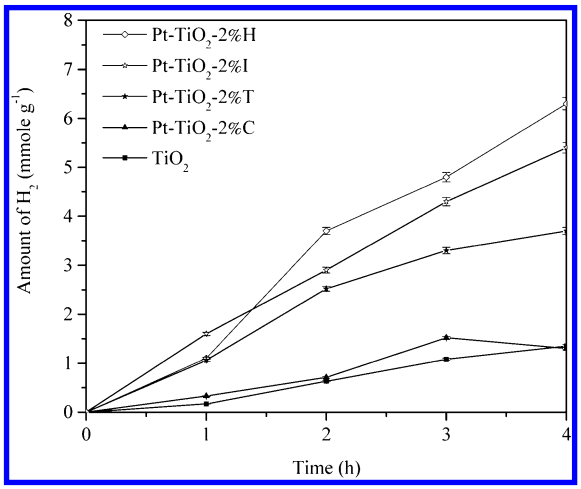

Figure 9. Photocatalytic hydrogen evolution from Pt−TiO_2 oxide materials; bare TiO_2 is also shown for comparison.

calculated for the Pt−TiO_2 materials prepared in this study by the hydrothermal, templated, core-like, and impregnation methods are shown in Table 1. The hydrothermally prepared Pt−TiO_2−2%H exhibited the highest hydrogen evolution rate of 6.3 mmol g^{-1} after 4 h of irradiation. The enhancement may be credited to high surface area (167 m^2/g), small crystallite size (7 nm), and the presence of high wt % of Pt^0 (37.6 wt %). As discussed later in the section related to EPR and PL studies, the critical parameter seems to be the large amounts of Pt^0 that minimizes electron−hole recombination to a significant extent than Pt−TiO_2−2%I, Pt−TiO_2−2%T, and Pt−TiO_2−2%C. Pt−TiO_2−2%I, Pt−TiO_2−2%T, Pt−TiO_2−2%C, and TiO_2 demonstrate hydrogen evolution rates of 5.4, 3.7, 1.3, and 1.4 mmol g^{-1}, respectively, after 4 h of irradiation.

It has been reported that the modification of TiO_2 surface with Pt enhanced the photocatalytic efficiency of TiO_2.[43,44] This may arise from the formation of a heterojunction (Schottky barrier) between TiO_2 and Pt species, leading to accelerated migration of photogenerated electrons to the noble metal particles.[45,46] Subsequently, this would decrease the electron−hole recombination and improve the photocatalytic activity.[46]

In this study, HTREM studies and the high density of elements shown in the EDX mappings indicate that the Pt species and TiO_2 are in intimate contact more favorably in the Pt−TiO_2−2%H and Pt−TiO_2−2%I, thus facilitating the formation of the heterojunctions. However, there is a difference in performance between both photocatalysts, and it may be attributed to differences in the amount of Pt (wt %) in these photocatalysts. Pt−TiO_2−2%H exhibits a higher hydrogen evolution rate of 6.3 mmol g^{-1} after 4 h of irradiation than Pt−TiO_2−2%I due to the higher wt % of Pt^0 of 37.6 wt % as compared to 15.5%. It is believed that the Pt^0 is more efficient to accept photogenerated electrons than their oxidized platinum counterparts, and thus the activity of Pt−TiO_2−2% H is higher than that of Pt−TiO_2−2%I.

Even though the XPS of Pt−TiO_2−2%T and the Pt−TiO_2−2%C suggests 100 wt % PtO_2 in both materials, Pt−TiO_2−2%T exhibits a higher evolution rate of 3.7 mmol g^{-1} than the 1.3 mmol g^{-1} evolved by Pt−TiO_2−2%C. HRTEM and EDX mapping studies indicate that the interactions between PtO_2 and TiO_2 are different in these two materials and may be the resultant cause of the varied hydrogen evolution rates. The PtO_2 and TiO_2 in Pt−TiO_2−2%T are in close enough contact for the viability of heterojunction formation. Because PtO_2 is a p-type semiconductor with a narrow band gap as compared to TiO_2,[47] we can argue that once the composite material is formed, the electrons that are generated by simulated solar light illumination can migrate from TiO_2 to PtO_2 due to their band edge difference in conduction band, thus prolonging the lifetime of hole−electron pairs in TiO_2 as reported previously.[22] Thus, PtO_2 can act as electron trap and increase the activity by reducing the electron−hole recombination. However, in Pt−TiO_2−2%C, the PtO_2 and TiO_2 are rather distant from each other, which reduce the chance for heterojunction formation between the metal and semiconductor species. This further lowers the ability for PtO_2 to accept the photogenerated electrons from TiO_2 in this composite. Hence, the photocatalytic hydrogen evolution activity of Pt−TiO_2−2%C is comparable to that of pure TiO_2 (1.4 mmol g^{-1}).

Not surprisingly, the control sample Pt−TiO_2−2%PD evolved 16.8 mmol g^{-1} of hydrogen. The high activity of this sample is attributed to the relative high amount of Pt^0 (50.5 wt %) that is present in this sample, and Figure S5 suggests the presence of multiple heterojunctions in this sample. This suggests that the photodeposition method is an effective method to prepare relatively high amounts of Pt^0 and that the reduction time and temperatures used in this study to prepare the photocatalysts Pt−TiO_2−2%H and Pt−TiO_2−2%I need to be further optimized to obtain greater amounts of Pt^0. This is beyond the scope of this work, because the focus of this work was to highlight the differences in the amount and/or oxidation state of Pt obtained through several synthetic approaches and its influence in solar hydrogen production.

We can infer from these studies that the presence of Pt^0 or PtO_2 or both species can act as effective hole−electron separators and improve the photocatalytic hydrogen evolution. The hole−electron separation is more effective with a high amount of reduced Pt species (Pt^0). The pure TiO_2 material shows low activity, which is associated with rapid electron−hole recombination due to the lack of suitable electron trap species.

In addition, the crystallite size of TiO_2 in Pt−TiO_2−2%H is the smallest (ca. 7 nm) in comparison to the other three photocatalysts, Pt−TiO_2−2%I, Pt−TiO_2−2%T, and Pt−TiO_2−2%C, which all have crystallite sizes in the range of 10−14. It has been reported that lower crystallite and particle sizes lead to greater photocatalytic activity due to minimized bulk recombination of charge carriers. However, if the crystallite (particle) sizes decrease too much, surface recombination predominates and the activity decreases. For example, it has been found that ca. 7 nm particle size of titania is optimal for

dx.doi.org/10.1021/jp405727k | J. Phys. Chem. C 2013, 117, 16850−16862

highest photocatalytic activity for the gas-phase photooxidation of tricholoroethylene, and our studies too suggest the same.[48] Thus, the higher activity of Pt−TiO_2−2%H could also be high due to this factor.[49] The crystallite size of TiO_2 in Pt−TiO_2−2%PD is 12 ± 2 nm.

The particles sizes of the Pt species could also affect the photocatalytic activities. Our HRTEM results indicate the particle sizes of Pt to be around 7 nm in both Pt−TiO_2−2%H and Pt−TiO_2−2%I, respectively. The particle size of Pt in Pt−TiO_2−2%PD was found to be in a fairly broad range of 6−12 nm.

The particle sizes of PtO_2 were estimated to be ∼7, ∼7−10, ∼6, and ∼7 nm in Pt−TiO_2−2%H, Pt−TiO_2−2%I, Pt−TiO_2−2%T, and Pt−TiO_2−2%C, respectively. Thus, it seems that the particles sizes of Pt and/or PtO_2 do not vary much, and this can be discounted as a factor affecting the photocatalytic activity.

To understand the role of PtO_2 further, the solar simulated photocatalytic hydrogen evolution from Pt−TiO_2−0.5%I, Pt−TiO_2−1%I, Pt−TiO_2−2%I is also plotted in Figure S5 of the Supporting Information. The respective hydrogen evolution rates were 7.5, 5.8, and 5.4 mmol g^{-1}, which suggests that a low loading of 0.5% is optimum for attaining a PtO_2/Pt^0 ratio at which the well-dispersed Pt species can form effective heterojunctions that facilitate electron migration, minimize charge recombination, and subsequently enhance photocatalytic hydrogen evolution. The absence of peaks due to Pt^0 species in the XRD of Pt−TiO_2−0.5%I alludes to more effective dispersion of Pt species as compared to the other two higher loaded composites prepared by the impregnation method. Hence, Pt−TiO_2−0.5%I shows slightly higher activity as compared to Pt−TiO_2−1%I and Pt−TiO_2−2%I.

3.8. Electron Paramagnetic Resonance (EPR) Studies. It is well documented that the magnitude of temperature treatment may have an influence on the formation and location of defect sites either on the surface or in the lattice of TiO_2 powders.[50] In addition, calcinations under reducing environment, that is, under H_2 flow both in the presence and in the absence of chloroplatinic acid, may result in the formation of structural defects such as oxygen vacancies in the titania.[51] It has been demonstrated previously that nonstoichiometry and the presence of partially reduced Ti both account for the photocatalysis in the presence of visible light.[52−55] Thus, we employed EPR spectroscopy to investigate the activity of the platinized TiO_2 samples under these conditions, through which the formation of photogenerated charge carriers was confirmed. The samples were dispersed in glycerol/water (1:1) solvent, bubbled with nitrogen, and illuminated for 10 min at 77 K using Xe lamp with 400 nm cut off filter. The EPR spectra were recorded at 5 K in dark immediately after illumination. Figure 10 presents the EPR spectra normalized to the sharp signal of organic radical from glycerol observed with g = 2.004 to compare relative trends. EPR spectra confirmed the formation of Ti^{3+} at g = 1.982 that is attributed to localized electrons on the bulk of anatase phase of titania.[51,56] The trend for the intensity of the signal decreases in the order of Pt−TiO_2−2%H > Pt−TiO_2−2%I > Pt−TiO_2−2%T > Pt−TiO_2−2%C, which is in very good agreement with the efficiency of hydrogen production. This can be explained not only by the different structure of platinized TiO_2, but by suppressed charge-carrier recombination and/or by the visible light photosensitization of possible platinum clusters, metallic Pt^0, and/or PtO_2[57] that have been clearly identified by XPS and HRTEM in this study.

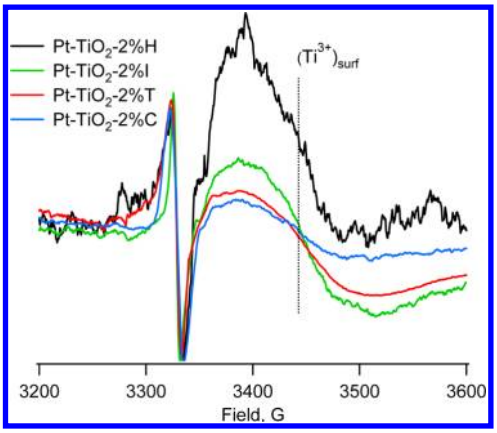

Figure 10. Normalized EPR spectra of Pt−TiO_2−2%H, TiO_2−2%I, Pt−TiO_2−2%T, and Pt−TiO_2−2%C, recorded in the dark at 5 K, after illumination at 77 K.

The EPR results indicate that the intensity of the signal due to Ti^{3+} is in the order Pt−TiO_2−2%H > Pt−TiO_2−2%I > Pt−TiO_2−2%T > Pt−TiO_2−2%C. The photocatalytic activity is also in the same order. While comparing the EPR signals due to Ti^{3+}, one can notice that the intensity of this signal is substantially higher in Pt−TiO_2−2%H in comparison to the other three samples. This can be attributed to the highest amount of Pt^0 in this sample that acts as an effective electron sink, minimizes electron−hole recombination, and stabilizes Ti^{3+} ions to a greater extent. Hence, the presence of high amounts of Pt^0 (37.6 wt %) in Pt−TiO_2−2%H leads to larger amounts of Pt−TiO_2 heterojunctions, which in turn leads to greater activity. Pt−TiO_2−2%I shows the second highest intensity due to Ti^{3+}. The XPS, HRTEM, and EDS results that are shown in Figure S4 indicate that this sample has 15.5 wt % Pt, and, in addition, close interaction of Pt and PtO_2 is indicated. The samples Pt−TiO_2−2%T and Pt−TiO_2−2%C have only PtO_2, and, as discussed previously, these two samples are less effective in trapping electrons and stabilizing Ti^{3+} ions and hence the ESR intensities of these two samples are relatively lower. Among these two samples, the activity of Pt−TiO_2−2%T is higher than that of Pt−TiO_2−2%C primarily due to the enhanced formation of heterojunctions in the former as compared to the later as evidence from the HRTEM and EDS studies and discussed previously. However, because the electron trapping nature of PtO_2 is much lower than that of Pt, the EPR studies indicate that the signals due to Ti^{3+} ions are lower and follow the same trend as the photocatalytic activities of these two samples.

Among all of the samples, Pt−TiO_2−2%H has the highest specific surface area as indicated in Table 1. In general, the higher is the specific surface area, the greater number of active sites per gram of samples and the specific surface area could also be a factor. However, as the EPR results indicate, the signal due to Ti^{3+} is much higher in this sample as compared to the other three samples with 2 wt % loadings of Pt species. This suggests that the electron trapping ability of Pt^0 due to the formation heterojunctions is the overriding factor and the surface area is not a significant factor.

The electronic properties due to different loadings of Pt and PtO_2 in the photocatalysts prepared by impregnation were also investigated, and the results are displayed in Figure S7 of the Supporting Information. Similar EPR features were observed for the photocatalysts prepared by the various aforementioned

methods. The strongest signal due to Ti^{3+} was observed for the low loaded Pt−TiO_2−0.5%I, followed by Pt−TiO_2−1%I and Pt−TiO_2−2%I. These observations are also consistent with photocatalytic efficiency results, thus emphasizing the necessity of an optimal loading of Pt species for enhanced rates of hydrogen evolution.

It is observed that the photocatalytic activity of Pt−TiO_2−0.5%I is the highest in this work among all of the samples prepared by thermal reduction. As the Pt loading is increased, other roles of Pt as a light shielder, pore blocker, recombination center for electrons and holes, and catalyst for recombining hydrogen and oxygen need to be considered. The light shielding effect, which is a combination of two factors due to absorption and scattering, may also play an important role. This can be understood by looking at Figure 8C and D. Among the I series of samples, one can notice that the absorbance of Pt−TiO_2−0.5%I in the 380−400 nm is slightly higher than that of the other two samples, Pt−TiO_2−1%I and Pt−TiO_2−2%I. Hence, as the Pt loading increases, these particles shield part of the incident light, and this may be one factor that is responsible for the enhanced activity of Pt−TiO_2−0.5%I. The pore blocking effect can be discounted because we do not see any correlation between the photocatalytic activity and the pore size of titania. The most important factor is the role of Pt in minimizing electron−hole recombination. This can be inferred from Figure S7 that shows the normalized EPR spectra in the I series of samples. It is clear that the EPR signal due to Ti^{3+} is higher in Pt−TiO_2−0.5%I in comparison to Pt−TiO_2−1%I and Pt−TiO_2−2%I. This clearly indicates that the Pt particles in Pt−TiO_2−0.5%I minimize charge-carrier recombination to a greater extent than Pt−TiO_2−1%I and Pt−TiO_2−2%I. As the Pt amounts increase, one notices a decrease in the signal due to Ti^{3+}, suggesting enhanced electron−hole recombination due to the enhanced negative charge on titania that offsets the charge separation efficacy effects of Pt. This is also consistent with the photoluminescence results as indicated in Figure S6. One notices an increase in the PL intensity as the loading of Pt is increased, suggesting enhanced electron−hole recombination. In addition, Pt is also known to act a recombination center for hydrogen and oxygen, and this could be another reason for the decrease in activity as the loadings are increased.

3.9. Photoluminescence (PL) Emission Studies. The PL emission spectrum is used to evaluate the efficiency of charge carrier trapping, migration, transfer, and separation to understand the fate of photogenerated electrons and holes in photocatalytic reactions. The emission spectra of Pt−TiO_2 composite materials along with bare TiO_2 are shown in Figure 11.The samples were excited at 385 nm, and the emission spectra were monitored in the 400−500 nm range, which is the typical emission range for TiO_2. All of the materials show comparable peak positions with variation in intensities. The emission band observed near 425 nm is attributed to the exciton-trapped shallow surface states.[58,59] The bands at 450 and 468 nm are attributed to band edge free excitons.[60,61] The bands at 482 and 493 nm are due to the bound excitons.[61] From the spectra, it is clear that the PL intensity of TiO_2 is reduced after the formation of Pt−TiO_2 composite materials. The PL intensities of Pt−TiO_2−2%H and Pt−TiO_2−2%I are lower as compared to Pt−TiO_2−2%T and Pt−TiO_2−2%C. The Pt−TiO_2−2%H shows the lowest PL intensity among the series studied, thus indicating relatively lower recombination rate of electrons and holes under identical experimental conditions.

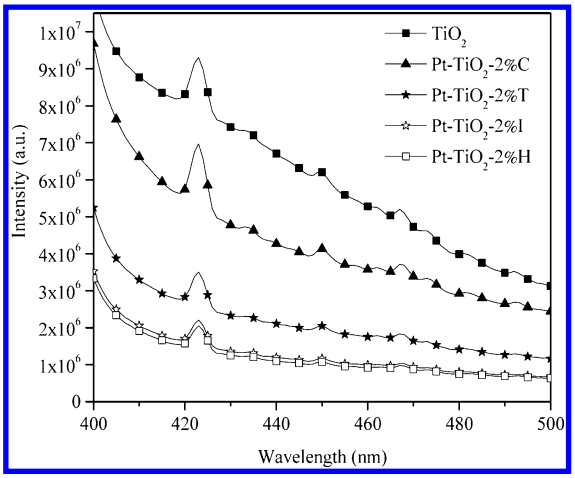

Figure 11. Photoluminescence emission spectra of Pt−TiO_2 composite materials; the bare TiO_2 is also shown for comparison.

The excited electrons can migrate to Pt^0 and/or PtO_2 from the conduction band of TiO_2 and retard the direct recombination of electrons and holes, thereby increasing the photocatalytic efficiency of Pt−TiO_2−2%H. Thus, the PL studies are consistent with the hydrogen evolution results.

Moreover, from HRTEM analysis, the Pt and PtO_2 are densely occupied on the TiO_2 surface and are in close contact with each other in Pt−TiO_2−2%H as compared to other materials. The composite Pt−TiO_2−2%I consists of a lower amount of Pt^0 as compared to Pt−TiO_2−2%H, and the Pt^0 and PtO_2 are existent in slightly lower density than in Pt−TiO_2−2% H on the TiO_2 surface. Therefore, Pt−TiO_2−2%I shows slightly higher recombination rate of the charge carriers, increased luminescence, and slightly lower photocatalytic activity. Because of the presence of heterojunction within these materials, Pt^0 or PtO_2 can effectively trap electrons.[47] Thus, the modification of TiO_2 with PtO_2 in Pt−TiO_2−2%T lowers the electron−hole recombination as compared to TiO_2, thereby exhibiting improved activity. From HRTEM and EDX elemental mapping, we observed that PtO_2 species present in Pt−TiO_2−2%C is more distant from TiO_2 as compared to that in Pt−TiO_2−2%T. Thus, PtO_2 is ineffective in trapping electrons in Pt−TiO_2−2%C, and, as a result, the activity of this material is reduced due to high electron−hole recombination as compared to that in Pt−TiO_2−2%T. It is clear that close contact between TiO_2 and Pt/PtO_2 is a major factor that contributes to the photocatalytic activity of the composite materials.

4. CONCLUSIONS

We prepared highly active Pt−TiO_2 composite photocatalyst materials by treating TiO_2 with platinum precursor using four different methods: hydrothermal, template, core-like, and impregnation. The Pt species in the resultant materials consist of different composition of reduced Pt^0 and PtO_2. Among the materials synthesized, the Pt−TiO_2−2%H prepared by hydrothermal treatment had the highest surface area, high Pt^0 wt %, and the presence of Pt−TiO_2 and PtO_2−TiO_2 heterojunctions were discerned from TEM studies. The photocatalyst exhibits a photocatalytic hydrogen evolution rate of 6.3 mmol g^{-1} catalyst after 4 h of solar simulated irradiation, whereas Pt−TiO_2−2%I, Pt−TiO_2−2%T, and Pt−TiO_2−2%C exhibit 5.4, 3.7, and 1.3 mmol g^{-1} under identical experimental conditions. These

dx.doi.org/10.1021/jp405727k | J. Phys. Chem. C 2013, 117, 16850−16862

results indicate that the presence of Pt^0 or PtO_2 in close contact with TiO_2 allows for more efficient electron propagation and facilitates minimization of electron−hole recombination, thus improving photocatalytic hydrogen evolution under simulated solar light irradiation. This work provides useful information regarding the influences of PtO_2−TiO_2 heterojunctions in solar simulated hydrogen production. It also provides scientific insight about preferential synthetic protocol for platinization of TiO_2, the effect of the heterojunction interaction of PtO_2 and Pt^0 with TiO_2, EDX mapping, HRTEM, EPR, and PL studies for the characterization of such photocatalytically active noble metal−semiconductor oxide materials.

■ ASSOCIATED CONTENT

Supporting Information

Additional figures. This material is available free of charge via the Internet at http://pubs.acs.org.

■ AUTHOR INFORMATION

Corresponding Author

*Tel.: 605-677-6189. Fax: 605-677-6397. E-mail: ranjit.koodali@usd.edu.

Notes

The authors declare no competing financial interest.

■ ACKNOWLEDGMENTS

This work was supported by DE-EE 0000270, NSF-CHE 0840507, NSF-CHE 0722632, and NSF-EPS 0903804. We are thankful to Dr. C. Jiang for Raman and Dr. J. Hoefelmeyer for TEM analysis. Use of the Center for Nanoscale Materials was supported by the U.S. Department of Energy, Office of Science, Office of Basic Energy Sciences, under Contract No. DE-AC02-06CH11357.

■ REFERENCES

(1) Izumi, Y. Recent Advances in the Photocatalytic Conversion of Carbon Dioxide to Fuels with Water and/or Hydrogen Using Solar Energy and Beyond. *Coord. Chem. Rev.* **2013**, *257*, 171−186.

(2) Barreca, D.; Carraro, G.; Gombac, V.; Gasparotto, A.; Maccato, C.; Fornasiero, P.; Tondello, E. Supported Metal Oxide Nanosystems for Hydrogen Photogeneration: Quo Vadis? *Adv. Funct. Mater.* **2011**, *21*, 2611−2623.

(3) Fujishima, A.; Honda, K. Electrochemical Photolysis of Water at a Semiconductor Electrode. *Nature* **1972**, *238*, 37−38.

(4) Mills, A.; Le Hunte, S. An Overview of Semiconductor Photocatalysis. *J. Photochem. Photobiol., A* **1997**, *108*, 1−35.

(5) Cho, K. C.; Hwang, K. C.; Sano, T.; Takeuchi, K.; Matsuzawa, S. Photocatalytic Performance of Pt-Loaded TiO_2 in the Decomposition of Gaseous Ozone. *J. Photochem. Photobiol., A* **2004**, *161*, 155−161.

(6) Driessen, M. D.; Grassian, V. H. Photooxidation of Trichloroethylene on Pt/TiO_2. *J. Phys. Chem. B* **1998**, *102*, 1418−1423.

(7) Ishibai, Y.; Sato, J.; Nishikawa, T.; Miyagishi, S. Synthesis of Visible-Light Active TiO_2 Photocatalyst with Pt-Modification: Role of TiO_2 Substrate for High Photocatalytic Activity. *Appl. Catal., B: Environ.* **2008**, *79*, 117−121.

(8) Kimura, K.; Einaga, H.; Teraoka, Y. Catalytic Properties of Platinum Supported on Titanium Dioxide by Liquid-Phase Adsorption of Colloidal Nanoparticles. *Catal. Lett.* **2010**, *139*, 72−76.

(9) Ohtani, B.; Iwai, K.; Nishimoto, S.; Sato, S. Role of Platinum Deposits on Titanium(IV) Oxide Particles: Structural and Kinetic Analyses of Photocatalytic Reaction in Aqueous Alcohol and Amino Acid Solutions. *J. Phys. Chem. B* **1997**, *101*, 3349−3359.

(10) Yang, J. C.; Kim, Y. C.; Shul, Y. G.; Shin, C. H.; Lee, T. K. Characterization of Photoreduced Pt/TiO_2 and Decomposition of Dichloroacetic Acid over Photoreduced Pt/TiO_2 Catalysts. *Appl. Surf. Sci.* **1997**, *121−122*, 525−529.

(11) Trillas, M.; Peral, J.; Domènech, X. Redox Photodegradation of 2,4-Dichlorophenoxyacetic Acid over TiO_2. *Appl. Catal., B: Environ.* **1995**, *5*, 377−387.

(12) Vorontsov, A. V.; Savinov, E. N.; Zhensheng, J. Influence of the Form of Photodeposited Platinum on Titania Upon Its Photocatalytic Activity in CO and Acetone Oxidation. *J. Photochem. Photobiol., A* **1999**, *125*, 113−117.

(13) Zhao, W.; Chen, C.; Li, X.; Zhao, J.; Hidaka, H.; Serpone, N. Photodegradation of Sulforhodamine-B Dye in Platinized Titania Dispersions under Visible Light Irradiation:Influence of Platinum as a Functional Co-Catalyst. *J. Phys. Chem. B* **2002**, *106*, 5022−5028.

(14) Sun, B.; Vorontsov, A. V.; Smirniotis, P. G. Role of Platinum Deposited on TiO_2 in Phenol Photocatalytic Oxidation. *Langmuir* **2003**, *19*, 3151−3156.

(15) Lee, J.; Choi, W. Effect of Platinum Deposits on TiO_2 on the Anoxic Photocatalytic Degradation Pathways of Alkylamines in Water: Dealkylation and N-Alkylation. *Environ. Sci. Technol.* **2004**, *38*, 4026−4033.

(16) Galińska, A.; Walendziewski, J. Photocatalytic Water Splitting over Pt−TiO_2 in the Presence of Sacrificial Reagents. *Energy Fuels* **2005**, *19*, 1143−1147.

(17) Furube, A.; Asahi, T.; Masuhara, H.; Yamashita, H.; Anpo, M. Direct Observation of a Picosecond Charge Separation Process in Photoexcited Platinum-Loaded TiO_2 Particles by Femtosecond Diffuse Reflectance Spectroscopy. *Chem. Phys. Lett.* **2001**, *336*, 424−430.

(18) Yamakata, A.; Ishibashi, T.; Onishi, H. Water- and Oxygen-Induced Decay Kinetics of Photogenerated Electrons in TiO_2 and Pt/TiO_2: A Time-Resolved Infrared Absorption Study. *J. Phys. Chem. B* **2001**, *105*, 7258−7262.

(19) Hufschmidt, D.; Bahnemann, D.; Testa, J. J.; Emilio, C. A.; Litter, M. I. Enhancement of the Photocatalytic Activity of Various TiO_2 Materials by Platinisation. *J. Photochem. Photobiol., A* **2002**, *148*, 223−231.

(20) Xie, Y.; Ding, K.; Liu, Z.; Tao, R.; Sun, Z.; Zhang, H.; An, G. In Situ Controllable Loading of Ultrafine Noble Metal Particles on Titania. *J. Am. Chem. Soc.* **2009**, *131*, 6648−6649.

(21) Teoh, W. Y.; Mädler, L.; Amal, R. Inter-Relationship between Pt Oxidation States on TiO_2 and the Photocatalytic Mineralisation of Organic Matters. *J. Catal.* **2007**, *251*, 271−280.

(22) Wang, H.; Wu, Z.; Liu, Y.; Wang, Y. Influences of Various Pt Dopants over Surface Platinized TiO_2 on the Photocatalytic Oxidation of Nitric Oxide. *Chemosphere* **2009**, *74*, 773−778.

(23) Lee, J.; Choi, W. Photocatalytic Reactivity of Surface Platinized TiO_2: Substrate Specificity and the Effect of Pt Oxidation State. *J. Phys. Chem. B* **2005**, *109*, 7399−7406.

(24) Kibombo, H. S.; Wu, C.-M.; Peng, R.; Baltrusaitis, J.; Koodali, R. T. Investigation of the Role of Platinum Oxide for the Degradation of Phenol under Simulated Solar Irradiation. *Appl. Catal., B: Environ.* **2013**, *136−137*, 248−259.

(25) Abe, T.; Suzuki, E.; Nagoshi, K.; Miyashita, K.; Kaneko, M. Electron Source in Photoinduced Hydrogen Production on Pt-Supported TiO_2 Particles. *J. Phys. Chem. B* **1999**, *103*, 1119−1123.

(26) Bamwenda, G. R.; Tsubota, S.; Nakamura, T.; Haruta, M. Photoassisted Hydrogen Production from a Water-Ethanol Solution: A Comparison of Activities of Au-TiO_2 and Pt-TiO_2. *J. Photochem. Photobiol., A* **1995**, *89*, 177−189.

(27) Kandiel, T. A.; Ismail, A. A.; Bahnemann, D. W. Mesoporous TiO_2 Nanostructures: A Route to Minimize Pt Loading on Titania Photocatalysts for Hydrogen Production. *Phys. Chem. Chem. Phys.* **2011**, *13*, 20155−20161.

(28) Chen, T.; Feng, Z.; Wu, G.; Shi, J.; Ma, G.; Ying, P.; Li, C. Mechanistic Studies of Photocatalytic Reaction of Methanol for Hydrogen Production on Pt/TiO_2 by *in Situ* Fourier Transform Ir and Time-Resolved Ir Spectroscopy. *J. Phys. Chem. C* **2007**, *111*, 8005−8014.

(29) Lakshminarasimhan, N.; Bokare, A. D.; Choi, W. Effect of Agglomerated State in Mesoporous TiO_2 on the Morphology of

Photodeposited Pt and Photocatalytic Activity. *J. Phys. Chem. C* **2012**, *116*, 17531−17539.
(30) Patsoura, A.; Kondarides, D. I.; Verykios, X. E. Photocatalytic Degradation of Organic Pollutants with Simultaneous Production of Hydrogen. *Catal. Today* **2007**, *124*, 94−102.
(31) Malinka, E. A.; Kamalov, G. L. Influence of Ph and Surface Complexes on the Rate Hydrogen Evolution from Photocatalytic Systems Pt/TiO_2-Electron Donor. *J. Photochem. Photobiol., A* **1994**, *81*, 193−197.
(32) Parayil, S. K.; Kibombo, H. S.; Wu, C. M.; Peng, R.; Baltrusaitis, J.; Koodali, R. T. Enhanced Photocatalytic Water Splitting Activity of Carbon-Modified TiO_2 Composite Materials Synthesized by a Green Synthetic Approach. *Int. J. Hydrogen Energy* **2012**, *37*, 8257−8267.
(33) Garcia-Martinez, J.; Linares, N.; Sinibaldi, S.; Coronado, E.; Ribera, A. Incorporation of Pd Nanoparticles in Mesostructured Silica. *Microporous Mesoporous Mater.* **2009**, *117*, 170−177.
(34) Kibombo, H. S.; Koodali, R. T. Heterogeneous Photocatalytic Remediation of Phenol by Platinized Titania−Silica Mixed Oxides under Solar-Simulated Conditions. *J. Phys. Chem. C* **2011**, *115*, 25568−25579.
(35) Lee, H.; Habas, S. E.; Kweskin, S.; Butcher, D.; Somorjai, G. A.; Yang, P. Morphological Control of Catalytically Active Platinum Nanocrystals. *Angew. Chem.* **2006**, *118*, 7988−7992.
(36) Parayil, S. K.; Kibombo, H. S.; Mahoney, L.; Wu, C. M.; Yoon, M.; Koodali, R. T. Synthesis of Mixed Phase Anatase-TiO_2(B) by a Simple Wet Chemical Method. *Mater. Lett.* **2013**, *95*, 175−177.
(37) Parayil, S. K.; Kibombo, H. S.; Koodali, R. T. Naphthalene Derivatized TiO_2−Carbon Hybrid Materials for Efficient Photocatalytic Splitting of Water. *Catal. Today* **2013**, *199*, 8−14.
(38) Kruk, M.; Jaroniec, M. Gas Adsorption Characterization of Ordered Organic−Inorganic Nanocomposite Materials. *Chem. Mater.* **2001**, *13*, 3169−3183.
(39) Lowell, S.; Shields, J. E.; Thomas, M. A.; Thommes, M. *Characterization of Porous Solids and Powders: Surface Area, Pore Size and Density*; Academic Press Inc.: San Diego, CA, 1990; Vol. *13*.
(40) Pitchon, V.; Fritz, A. The Relation between Surface State and Reactivity in the $Deno_x$ Mechanism on Platinum-Based Catalysts. *J. Catal.* **1999**, *186*, 64−74.
(41) Chen, C. A.; Chen, Y. M.; Huang, Y. S.; Tsai, D. S.; Tiong, K. K.; Liao, P. C. Synthesis and Characterization of Well-Aligned Anatase TiO_2 Nanocrystals on Fused Silica Via Metal-Organic Vapor Deposition. *CrystEngComm* **2009**, *11*, 2313−2318.
(42) Chen, X.; Mao, S. S. Titanium Dioxide Nanomaterials: Synthesis, Properties, Modifications, and Applications. *Chem. Rev.* **2007**, *107*, 2891−2959.
(43) Wang, C.; Yin, L.; Zhang, L.; Liu, N.; Lun, N.; Qi, Y. Platinum-Nanoparticle-Modified Tio_2 Nanowires with Enhanced Photocatalytic Property. *ACS Appl. Mater. Interfaces* **2010**, *2*, 3373−3377.
(44) Zou, J. J.; Chen, C.; Liu, C. J.; Zhang, Y. P.; Han, Y.; Cui, L. Pt Nanoparticles on TiO_2 with Novel Metal−Semiconductor Interface as Highly Efficient Photocatalyst. *Mater. Lett.* **2005**, *59*, 3437−3440.
(45) Linsebigler, A. L.; Lu, G.; Yates, J. T. Photocatalysis on TiO_2 Surfaces: Principles, Mechanisms, and Selected Results. *Chem. Rev.* **1995**, *95*, 735−758.
(46) Zeng, H.; Cai, W.; Liu, P.; Xu, X.; Zhou, H.; Klingshirn, C.; Kalt, H. ZnO-Based Hollow Nanoparticles by Selective Etching: Elimination and Reconstruction of Metal−Semiconductor Interface, Improvement of Blue Emission and Photocatalysis. *ACS Nano* **2008**, *2*, 1661−1670.
(47) Hass, K. C.; Carlsson, A. E. Band Structures of Nonmagnetic Transition-Metal Oxides: Pdo and Pto. *Phys. Rev. B* **1992**, *46*, 4246−4249.
(48) Almquist, C. B.; Biswas, P. Role of Synthesis Method and Particle Size of Nanostructured TiO_2 on Its Photoactivity. *J. Catal.* **2002**, *212*, 145−156.
(49) Rungjaroentawon, N.; Onsuratoom, S.; Chavadej, S. Hydrogen Production from Water Splitting under Visible Light Irradiation Using Sensitized Mesoporous-Assembled TiO_2-SiO_2 Mixed Oxide Photocatalysts. *Int. J. Hydrogen Energy* **2012**, *37*, 11061−11071.
(50) Liu, H.; Ma, H. T.; Li, X. Z.; Li, W. Z.; Wu, M.; Bao, X. H. The Enhancement of TiO_2 Photocatalytic Activity by Hydrogen Thermal Treatment. *Chemosphere* **2003**, *50*, 39−46.
(51) Vijayan, B. K.; Dimitrijevic, N. M.; Wu, J.; Gray, K. A. The Effects of Pt Doping on the Structure and Visible Light Photoactivity of Titania Nanotubes. *J. Phys. Chem. C* **2010**, *114*, 21262−21269.
(52) Komiyama, M.; Li, Y.-J. Photoresponse of Surface Oxygen Defects on TiO_2(110). *Appl. Surf. Sci.* **2005**, *244*, 550−553.
(53) Chen, L.; Graham, M. E.; Li, G.; Gentner, D. R.; Dimitrijevic, N. M.; Gray, K. A. Photoreduction of Co_2 by TiO_2 Nanocomposites Synthesized through Reactive Direct Current Magnetron Sputter Deposition. *Thin Solid Films* **2009**, *517*, 5641−5645.
(54) Lo, H.-H.; Gopal, N. O.; Ke, S.-C. Origin of Photoactivity of Oxygen-Deficient TiO_2 under Visible Light. *Appl. Phys. Lett.* **2009**, *95*, 083126−083129.
(55) Nishikawa, M.; Sakamoto, H.; Nosaka, Y. Reinvestigation of the Photocatalytic Reaction Mechanism for Pt-Complex-Modified TiO_2 under Visible Light Irradiation by Means of ESR Spectroscopy and Chemiluminescence Photometry. *J. Phys. Chem. A* **2012**, *116*, 9674−9679.
(56) Bonneviot, L.; Haller, G. L. Epr Characterization of Ti^{3+} Ions at the Metal-Support Interface in Pt-TiO_2 Catalysts. *J. Catal.* **1988**, *113*, 96−105.
(57) Li, F. B.; Li, X. Z. The Enhancement of Photodegradation Efficiency Using Pt−TiO_2 Catalyst. *Chemosphere* **2002**, *48*, 1103−1111.
(58) Daude, N.; Gout, C.; Jouanin, C. Electronic Band Structure of Titanium Dioxide. *Phys. Rev. B* **1977**, *15*, 3229−3235.
(59) Jeon, K. S.; Oh, S. D.; Suh, Y. D.; Yoshikawa, H.; Masuhara, H.; Yoon, M. Blinking Photoluminescence Properties of Single TiO_2 Nanodiscs: Interfacial Electron Transfer Dynamics. *Phys. Chem. Chem. Phys.* **2009**, *11*, 534−542.
(60) Yu, J.; Yue, L.; Liu, S.; Huang, B.; Zhang, X. Hydrothermal Preparation and Photocatalytic Activity of Mesoporous Au−TiO_2 Nanocomposite Microspheres. *J. Colloid Interface Sci.* **2009**, *334*, 58−64.
(61) Yu, J.; Qi, L.; Jaroniec, M. Hydrogen Production by Photocatalytic Water Splitting over Pt/TiO_2 Nanosheets with Exposed (001) Facets. *J. Phys. Chem. C* **2010**, *114*, 13118−13125.